Microfluidics and Nanofluidics (2025) 29:70
https://doi.org/10.1007/s10404-025-02845-0

RESEARCH

Microfluidic mixing by micropost-driven acoustic microstreaming: effects of micropost shape, actuation voltage, and fluid flow rate

Bahareh Chaichypour[1,2,3] · Sinthuran Jegatheeswaran[2,3,4] · Alinaghi Salari[5,6] · Zjardyn L. Hood[7] · Aaron R. Wheeler[5,6,8] · Dae Kun Hwang[2,3,4] · Michael C. Kolios[1,2,3] · Scott S. H. Tsai[2,3,9]

Received: 4 April 2025 / Accepted: 8 September 2025 / Published online: 22 September 2025

Abstract

We describe an approach to enhancing microfluidic mixing by generating acoustic microstreaming flows around microposts in a microfluidic device. Specifically, we synthesize microposts with various cross-sectional shapes (i.e., circles, triangles, and stars) using photocrosslinkable polymers, allowing for precise control over their geometry. We also ensure unobstructed micropost vibration via carefully designed gaps between the microposts and the channel ceiling. Experimental findings reveal that the shape of microposts is critical in influencing microstreaming patterns and mixing efficiency. Circular microposts generate semi-symmetrical circular vortices, resulting in superior mixing performance (86.7%). In contrast, star-shaped microposts, despite having sharper edges and forming pairs of microvortices around their vertices, produce the lowest mixing performance (56.5%). This trend correlates with the microposts' moment of inertia (MOI); circular posts exhibit the lowest MOI and thus oscillate more readily, whereas star-shaped posts are geometrically more resistant to bending, limiting vibration amplitude and reducing streaming strength. Further characterization of the microstreaming flow patterns in a static aqueous solution reveals that the lower mixing performance of star-shaped micropillars is likely due to the impact of the spacing between the microposts and the emergence of counter-rotating pairs of microvortices, leading to destructive interference. Triangular microposts exhibit moderate mixing performance, generating a pair of opposing vortices around each vertex. Increasing the actuation voltage and reducing the flow rates further improves mixing across all micropost shapes. These findings highlight the significance of micropost design and arrangement in enhancing the performance of microfluidic acoustic mixers.

1 Introduction

Microfluidic devices find applications in various fields, including biomedicine and chemistry, owing to their small dimensions, reduced reagent consumption, and high surface-to-volume ratio (Beebe et al. 2002; Ebadi et al. 2019). However, in microfluidic devices, where laminar flow is dominant, the mixing of fluids is primarily driven by diffusion, which is a slow process resulting in inefficient mixing. This limitation can be understood by examining

✉ Scott S. H. Tsai
scott.tsai@torontomu.ca

1 Department of Physics, Toronto Metropolitan University, Toronto, ON M5B 2K3, Canada

2 Keenan Research Centre for Biomedical Science, St. Michael's Hospital, Toronto, ON M5B 1T8, Canada

3 Institute for Biomedical Engineering, Science and Technology (iBEST)—a partnership between Toronto Metropolitan University and St. Michael's Hospital, Toronto, ON M5B 1T8, Canada

4 Department of Chemical Engineering, Toronto Metropolitan University, Toronto, ON M5B 2K3, Canada

5 Terrence Donnelly Centre for Cellular & Biomolecular Research, University of Toronto, Toronto, ON M5S 3E1, Canada

6 Department of Chemistry, University of Toronto, Toronto, ON M5S 3H6, Canada

7 Department of Biology, University of Waterloo, Waterloo, ON N2L 3G1, Canada

8 Institute of Biomedical Engineering, University of Toronto, Toronto, ON M5S 3E2, Canada

9 Department of Mechanical, Industrial and Mechatronics Engineering, Toronto Metropolitan University, Toronto, ON M5B 2K3, Canada

two key non-dimensional numbers: the Reynolds number, Re, and the Peclet number, $Pe = \frac{UL}{D}$ (Stroock et al. 2002). The Reynolds number, which compares inertial to viscous forces, is typically near or below unity in microfluidics, reflecting laminar flows that have negligible inertial effects. The Peclet number, which compares convective to diffusive transport, is generally high, indicating that diffusion across streamlines is limited. Due to the low Reynolds number and high Peclet number associated with microfluidic flows, mixing of different solutions in microfluidics tends to be slow. As a result of this challenge, microfluidic micromixers have often been proposed, which increase the interfacial area between fluid streams using active or passive perturbation strategies to enhance mixing.

There are two main approaches to achieving improved mixing in microfluidic devices. The first approach is active mixing, where an external field or force is applied to augment the interfacial area between the fluid streams. The second approach is passive mixing, which involves designing the channel with obstacles or specific geometries that folds or convolutes the fluid streams, effectively increasing the diffusion area between the streams (Beebe et al. 2002; Lee et al. 2011; Li et al. 2022). Active methods, such as those utilizing magnetic (Hejazian et al. 2017), acoustic (Chen et al. 2022; Lu et al. 2018), and electric (Salari and Dalton 2019; Wu et al. 2022; Yang et al. 2021) principles, induce strong chaotic flows within the microfluidic system. Acoustic micromixers, in particular, are recognized for being contact-free, non-invasive, tunable, cost-effective, and highly precise (Chen et al. 2022).

A time-averaged acoustic microstreaming flow (which usually forms circular microvortices) is due to a non-linear effect resulting from harmonic oscillations in the coupling between a solid structure and the surrounding fluid dynamics (Nama et al. 2016). Most acoustic micromixers utilize embedded microstructures—such as sharp edges or trapped microbubbles—within the microfluidic channel to induce acoustic streaming under ultrasound excitation (Cha et al. 2023; Chen et al. 2022; Li et al. 2022). Alternatively, acoustic micromixers can be classified by the type of acoustic wave employed: bulk acoustic waves (BAW) or surface acoustic waves (SAW).

In BAW-based micromixers, pressure waves propagate through the bulk of the fluid or the channel wall, often forming standing wave fields that enable efficient particle manipulation and mixing. BAW-based configurations can employ either bulk piezoelectric actuators or thin-film piezoelectric layers (e.g., AlN, ZnO) integrated onto substrates, allowing compatibility with compact or CMOS-based microfluidic platforms (Nair et al. 2022; Zaheri-Ghannad et al. 2024). On the other hand, SAW-based micromixers use interdigitated transducers (IDTs) patterned on piezoelectric substrates such as lithium niobate ($LiNbO_3$) or lithium tantalate ($LiTaO_3$) to generate surface acoustic waves along the substrate surface. The resulting surface waves induce strong, localized streaming in adjacent fluid regions, offering precise control over targeted areas within the microchannel. SAW devices can incorporate single or paired IDTs in parallel, focused, or slanted arrangements to tailor flow profiles and enhance mixing performance (Ahmed 2019; Luong 2010; Zhang et al. 2019). Although SAW-based systems often achieve higher mixing efficiency compared to pillar- or bubble-based mixers, cleanroom fabrication and precise alignment of costly IDTs are typically required, which limits its accessibility (Ma et al. 2016; Zhou et al. 2016). Increased energy input may also lead to substrate and fluid heating, potentially compromising temperature-sensitive biological applications. Mixing performance in both BAW and SAW systems is strongly influenced by actuation voltage, frequency, and flow rate (Lim et al. 2019).

In acoustic micromixers with sharp edges, an array of sharp-edge microstructures is typically fabricated along the channel walls. It has been shown that increasing the number of sharp edges enhances the number of mixing sites, improving mixing efficiency (Zhao et al. 2021). Additionally, a sharper tip (smaller angle) of the sharp edge structure results in larger vibrational displacements at the tip, consequently generating stronger microstreaming, leading to more efficient mixing (Tian et al. 2018). Sharp edges with greater heights produce larger vibration displacements, further facilitating mixing (Zhao et al. 2021). Transducer characteristics, actuation parameters, and the rate and properties of the externally supplied flows are also among the factors that can potentially influence overall mixing performance. For instance, higher actuation voltages can produce larger oscillations and stronger microstreaming flows, thereby enhancing mixing efficiency (Huang et al. 2013; Tian et al. 2018). Additionally, the ratio between the rate of externally supplied flows and the microstreaming flow can influence mixing efficiency. A lower ratio enhances mixing efficiency by increasing fluid residence time in the mixing region, although it may reduce device throughput (Tian et al. 2018).

In bubble-based acoustic micromixers, once bubbles are formed in the device, transducer-driven actuation induces a circulating flow (comprising microvortices) around the gas-liquid interface of the bubble, a phenomenon known as cavitation microstreaming (Ahmed et al. 2009, 2016; Orbay et al. 2017; Xie et al. 2016). This disrupts the interface of the flows, facilitating mixing. Notably, slanted sharp edges with empty volumes in between have been utilized to form bubbles, leveraging the combined effects of both bubbles and sharp edges to enhance mixing. The synergistic effect of

both has proven more effective than employing each separately (Rasouli and Tabrizian 2019).

Aside from the more conventional acoustic micromixing techniques discussed above, other approaches have also been explored to improve acoustic mixing performance in microfluidics. One study, for instance, utilizes photocrosslinkable polymers to create artificial cilia inside a microfluidic channel. These cilia possess a fixed attachment at one end while remaining free at the other, and the acoustically-induced oscillation of the cilia enhances fluid mixing (Orbay et al. 2018). Another study highlighting recent advancements in acoustofluidic Manipulation demonstrates the potential of 3D microstructures to influence microstreaming in microfluidic systems, offering flexibility for various applications (Harley et al. 2024). The authors use the two-photon polymerization technique to fabricate microposts and to characterize a design parameter, namely the tip angle, on the microstreaming around isolated microposts with star and circular cross-sections. (Harley et al. 2024).

Despite these promising results, several key questions remain unanswered. Specifically there is a limited understanding of how the geometry of 3D microstructures in an acoustic field influences microstreaming patterns. Additionally, it remains unclear whether an array of single or multiple rows of closely packed structures can enhance the overall net flow in a manner different from that of individual structures—an effect that could significantly influence mixing efficiency.

Our work addresses these gaps by systematically studying these effects in an array of 3D microposts. Specifically, our study investigates the influence of micropost shape (circle, triangle, and star) and the interaction between neighbouring microposts on the resulting microstreaming patterns. This array-based approach allows us to explore how neighbouring microposts influence microstreaming patterns, an important aspect overlooked in earlier research. Additionally, while a previous study (Harley et al. 2024) primarily concentrates on microstreaming patterns, our study applies these fundamentals to a practical application—using microstreaming around 3D microposts to manipulate fluid for enhanced mixing efficiency. We also explore how varying flow parameters and actuation voltages influence mixing performance by enhancing microstreaming effects. Furthermore, we introduce an approach for synthesizing microposts with photocrosslinkable polymers within microchannels for acoustic micromixing applications. This approach offers significant flexibility, allowing researchers to tailor the shape, size, and material properties of the microposts to suit specific needs.

The developed device is designed to operate effectively in microchannels with high aspect ratios (i.e., large width-to-height ratios), which are beneficial for enhancing particle manipulation and mixing. Such channels increase the surface-to-volume ratio, promoting improved mass transfer and faster reaction kinetics—factors essential for efficient biochemical processes. Mixing performance in this system is influenced not only by actuation voltage and flow rate but also by the geometry of internal features such as microposts. By systematically varying micropost shapes, our study aims to reveal how structural design affects microstreaming behavior and overall mixing efficiency, providing insight into the development of more effective acoustofluidic mixing strategies.

2 Methods and materials

A. Microfluidic device fabrication

As illustrated in Fig. 1 (Steps 1–3) a Y-shaped microfluidic Channel was designed and fabricated with two inlets and one outlet. Each side Channel has a width of 500 μm, while the main channel is $400\ \mu$m in width. The height of the entire Y-shape channel is $60\ \mu$m. The channel was fabricated using the standard photolithography and soft lithography methods (Xia et al. 1998).

In Step 1, a silicon wafer was first coated with SU8 photoresist, exposed to UV light through a photomask, and developed to form a mold for casting polydimethylsiloxane (PDMS) replicas of the microfluidic channel. In Step 2, PDMS was prepared by mixing Sylgard 184 base and curing agent (Dow Corning, USA) in a 10:1 ratio, degassed, poured over the mold, and cured at 70 °C for 1 h. The cured PDMS was peeled off the mold and uniformly cut for various microfluidic devices (Salari et al. 2021; Xia and Whitesides 1998). Inlets and the outlet for the microfluidic device were created using a 1-mm biopsy punch (Integra Miltex USA). In Step 3, the PDMS device is bonded to a cover glass with a length of 50 mm and a width of 22 mm (No. 00, Agar Scientific, UK). Both surfaces were activated using air plasma (PDC32G, Harrick Plasma, USA) for ~30 s and immediately pressed together to form an irreversible seal. The PDMS channel was positioned parallel to the length of the cover glass, with the channel centerline approximately 3 mm from the edge. An acoustic transducer (7BB-27-4L0, Mouser Electronics, USA) with dimensions of 27 mm × 0.54 mm and a resonance frequency of 4.6 kHz, was then attached beside the microfluidic device. Approximately half of the transducer's bottom surface was bonded to the top surface of the cover glass using liquid PDMS and cured at 70 °C for 20 min (Salari et al. 2020, 2021).

B. Micropost synthesis

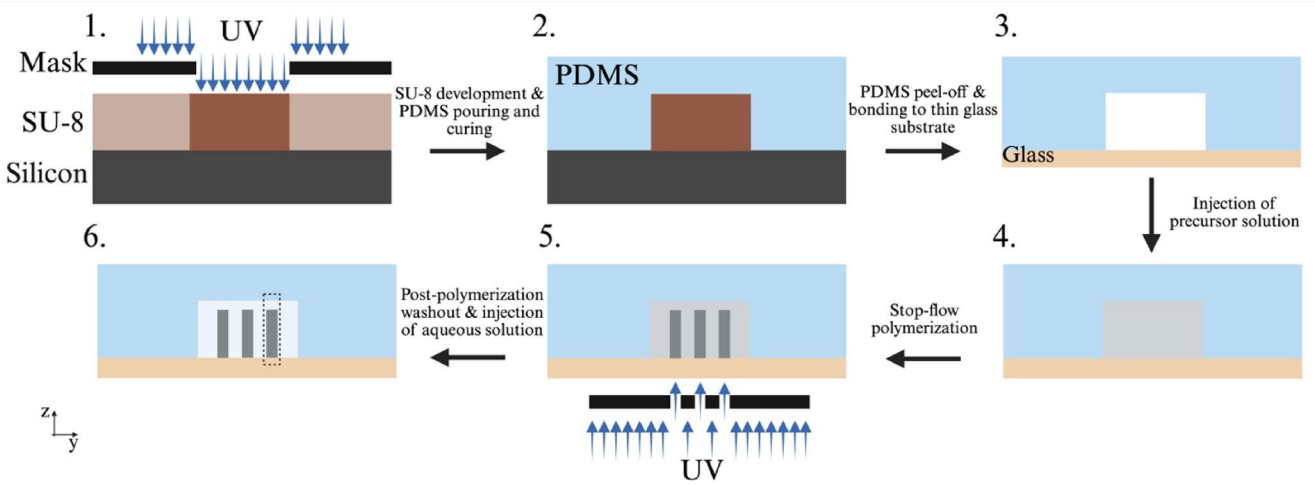

Fig. 1 Schematic illustration of the device fabrication and in situ micropost synthesis. Steps 1–3: Fabrication of the microfluidic channel by photolithography and softLithography. Steps 4 –6: Stop-flow lithography for micropost fabrication inside the channel

As illustrated in Steps 4–6 of Fig. 1, microposts were fabricated directly within the microfluidic channel using stop-flow lithography (Li 2015; Li et al. 2017; Moon et al. 2015). Prior to polymerization, the channel was treated in a plasma etcher at 30 W for 5 min. This was followed by surface modification, where a 2 wt% silane coupling solution—3-(Trimethoxysilyl)propyl methacrylate (Sigma Aldrich, USA) mixed with deionized (DI) water—was injected into the channel. The device was then incubated at room temperature for 2 hours to facilitate surface functionalization.

In Step 4, the channel was filled with a photocurable prepolymer solution consisting of 90 % polyethylene glycol diacrylate (PEGDA250) and 10% photoinitiator (2-hydroxy-2-methylpropiophenone), both from Sigma Aldrich, USA. In Step 5, the device was exposed to UV light at an intensity of approximately 11 $\frac{W}{cm^2}$ through a high-resolution photomask using an inverted microscope (Zeiss, Germany). The photomask (printed at 25,400 dpi, with a minimum feature size ~ 8 μm) was aligned such that only a ~ 290 μm × 290 μm area—corresponding to a single 3 × 3 micropost array—was illuminated at a time through the 20× objective lens. Proper alignment during photopolymerization was identified as a critical Step to achieve an array of symmetric microposts aligned to the channel. UV exposure induced the polymerization and curing of the prepolymer solution, resulting in solidified microposts with dimensions specified by the photomask.

Exposure was carried out sequentially along the length of the microchannel, with the exposure time optimized to 150 ms to ensure accurate and consistent micropost polymerization. Shorter exposure times resulted in underdeveloped structures with diameters below 60 μm, whereas longer exposures led to overgrowth due to excessive free radical diffusion, increasing both the outer soft layer and the overall diameter of microposts.

Finally, in Step 6, the channel was thoroughly flushed with a mixture of ethanol and DI water to remove any unreacted prepolymer and residual contaminants (Yuk et al. 2016). Each device contained microposts with a uniform height of approximately 56 μm and equal cross-sectional areas, with shapes including circles, triangles, and stars. High magnification scanning electron microscopy (SEM) was performed to evaluate the quality of the fabricated microposts. Representative top- and tilted-view images of circular microposts are provided in Supplementary Figure S1. While most microposts exhibited smooth profiles consistent with the photomask design, occasional fabrication-related imperfections such as edge irregularities, surface debris, or partial polymer residues were observed. These features appeared infrequently and are likely attributed to inherent limitations in the photopolymerization and development processes. Microposts were arranged in one, two, or three rows, symmetrically aligned along the channel width. The center-to-center distance between microposts along the channel length was 230 μm for devices with one or two rows, and 115 μm for devices with three rows. Across the channel width, this distance was 230 μm for two-row devices and 115 μm for three-row devices.

For our acoustofluidic experiments, we designed and fabricated microposts with three distinct cross-sectional shapes—circular, triangular, and star-shaped. The circular microposts were designed with a 60 μm diameter, while the triangular and star-shaped microposts were designed to have the same volume, approximately 169,000 μm^3 across all shapes, ensuring that any observed differences in microstreaming arise from shape alone rather than variations in other micropost properties.

C. Device operation

The completed acoustofluidic device was placed on the stage of an inverted microscope (Zeiss – Axio Observer D1, Germany) with the two widths of the cover glass secured on the stage. The microscope was equipped with a high-speed camera (Phantom Miro, Vision Research, USA). To excite the transducer, rectangular-shaped waves were created using a function generator (Agilent 33521A, USA) and amplified using a radio frequency power amplifier (Model: 2100 L, T&C Power Conversion, USA) with a fixed gain of 55 dB. During experiments, the device was actuated with a peak-to-peak voltage ranging from 0 V to 130 V at a fixed frequency of 98 kHz. The applied voltage was measured using a high-voltage oscilloscope probe (P6015A, Tektronix, USA) connected to a digital oscilloscope (TDS 2012B, Tektronix, USA). Rectangular waveform signals were chosen over sinusoidal ones because they produced stronger mixing performance under our specific experimental setup, where the transducer is bonded to the glass substrate beneath the microfluidic channel. This enhanced mixing was confirmed experimentally by comparing both waveforms at identical frequencies and voltages, as presented in Supplementary Figure S2. The effectiveness of step-function signals has also been supported in previous acoustofluidic studies, further validating our waveform selection (Lu et al. 2024).

To determine enhanced performance of microfluidic acoustic mixers operating 98 kHz, we performed a frequency sweep and found that microstreaming occurred only at specific resonance frequencies of the coupled system, rather than at the transducer's inherent resonance (4.6 kHz). Operating at 4.6 kHz resulted in large substrate oscillations and imaging instability. In contrast, 98 kHz consistently produced strong and stable microstreaming without substrate damage. Mixing performance measured at 33 kHz, 50 kHz, and 98 kHz further validated enhanced performance at 98 kHz, yielding the highest efficiency. Microstreaming videos and the corresponding mixing performance plot are provided in the supplementary material (Figure S3, Video S1 – S3).

To reduce the heating caused by high actuation voltages, we used pulsed acoustic actuation with a repetition period of 60 s— consisting of 3 s of "on" time followed by 57 s of "off" time. This approach, implemented through the burst mode on the function generator, helped mitigate heating effects induced by continuous high-voltage excitation. Thermal measurements using an infrared (IR) thermometer showed that under 118 V_{pp} actuation, the temperature of the PZT rose from ~26 °C (baseline) to ~38 °C during the 3-second pulse and subsequently decreased to ~30 °C during the 57-second rest period. Furthermore, we conducted experiments at lower actuation voltage. As expected, the strength of the microstreaming (i.e., the streaming velocity) decreased with lower voltages; however, the pattern of the microstreaming flow remained consistent. These results suggest that the observed microstreaming behavior is primarily driven by acoustic actuation rather than thermally induced effects. A representative microstreaming pattern around an oscillating circular micropost at low actuation voltage (31 V_{pp}) is shown in Supplementary Figure S4.

To prevent the introduction of bubbles into the channel, each PDMS device was treated with plasma (Harrick Plasma, USA) etcher for approximately 5 min at the beginning of the experiment, rendering it hydrophilic. Following plasma activation, deionized water was immediately introduced and continuously flowed through the channel to maintain wettability and minimize air bubble formation. Most experiments were completed on the same day. While some devices were reused for up to five experiments, no visible signs of degradation or significant changes in mixing performance were observed within this usage range. However, the long-term limit of device reuse was not systematically evaluated and may depend on factors such as storage conditions and experimental duration, and PZT degradation. Liquid injection into each of the two inlets was carried out using a syringe pump (Harvard Apparatus, USA) at a flow rate ranging from 5.0 to 16.7 µl/min, resulting in a total flow rate in the main channel ranging from 10.0 to 33.4 µl/min. Silicone tubes (Saint-Gobain, USA) were used to deliver the liquids to the inlets and remove the waste from the outlet (Figure S5).

In the microstreaming flow visualization experiments, polystyrene beads (1 µm, Polysciences, USA) served as tracers and were mixed with DI water and injected into both inlets. In mixing experiments, DI water spiked with blue dye was introduced through one inlet, while pure DI water was injected through the other inlet.

D. Data collection and analysis

In each experiment, two 16.8-second videos were recorded at a frame rate of 24 frames per second from regions near the entrance and exit of the main channel. Each video was sufficiently long to capture the fluid flow before, during, and after each acoustic pulse. Snapshot images were extracted from the videos for analysis. Each measurement corresponds to a separate acoustic pulse performed on the same device under identical conditions, with sufficient delay between pulses to avoid carryover effects. Although the measurements were conducted on the same device, they were performed independently and treated as separate experiments.

For flow visualization, tracer beads were tracked in the extracted video frames using the TrackMate plugin in ImageJ (Ershov et al. 2022). For mixing experiments, a

custom R script was used to automatically calculate the standard deviations of pixel intensities along a line across to the channel width in each frame. The R script (Supplementary File 1) was used to quantify mixing performance using the expression, $\varphi = 1 - \frac{\sigma}{\sigma_0}$, where σ_0 and σ are the standard deviation values associated with the entrance and exit of the main channel, respectively (Cai et al. 2017; Juraeva and Kang 2023; Li et al. 2022; Lu et al. 2024, 2023; Pothuri et al. 2019; Raza et al. 2020; Tsai and Wu 2011; Wang et al. 2021). MATLAB (MathWorks, USA) was used to curve-fit the mixing experimental data, as it provides a robust and flexible environment for implementing custom nonlinear models with multiple fitting parameters. The optimization and curve fitting toolboxes allowed precise definition of model equations and efficient multi-parameter fitting with control over convergence criteria and error analysis.

3 Results and discussion

A. Acoustic micromixer overview

As described earlier, we fabricate a Y-shaped microfluidic device using standard photolithography followed by soft-lithography, with microposts synthesized via the stop-flow lithography method (Fig. 1). We utilize stop-flow lithography because this method enables the base of each micropost to bond to the cover glass while the top remains free, due to oxygen inhibition of polymerization caused by diffusion through the porous PDMS (Fig. 1, Steps 4–6) (Debroy et al. 2018). As a result, the microposts function as cantilevers, allowing the top end to vibrate more freely (Fig.2a), unlike conventional microposts in microfluidic channels that are fixed at both ends (Kim et al. 2018; Park et al. 2014; Pawinanto et al. 2020). Also, this fabrication method produces microposts with a cylindrical geometry, as seen in the tilted-view, high-magnification SEM image (Fig.2a, z-y plane; Figure S1.c) (Hakimi et al. 2014).

After attaching the acoustic transducer and assembling the acoustofluidic device on the microscope stage, we continuously load the device with a dyed and a non-dyed aqueous solution through the two inlets, respectively (Figure S5 and Fig. 2b). Videos are recorded near the entrance and exit of the main channel, as shown in schematics in Fig. 2c(i) and 2c(iii), respectively.

Without the actuation of the transducer, fluid mixing in the main channel primarily occurs through diffusion. Upon transducer actuation, vibrations propagate through the cover glass to the PDMS channel, where they impact all objects, including the microposts. These vibrations lead to the formation of microstreaming flows, or microvortices, around the microposts, enabling the mixing of the two fluids in the main channel. Figure 2c further illustrates this process through three sections of the device: (i) near the inlets, where the fluids remain mostly unmixed across the channel width; (ii) in the main channel, where rotational flows, indicated by counterclockwise arrows, are generated around the microposts due to the acoustic vibrations. This microstreaming flow disrupts the interface between the two fluid streams, enhancing mixing across the width and along the length of the microfluidic channel. However, mixing across the width is of particular importance in our setup, as it introduces a short-range advective flow in an otherwise diffusion-limited direction. Section (iii) shows the region near the outlet of the channel, where complete mixing potentially occurs because of sufficiently strong acoustic microstreaming effects.

B. Characterizing the acoustic mixer

In our acoustofluidic device, fluid mixing is governed by the interaction between externally supplied laminar flows and acoustically induced microstreaming. When the transducer is off, only passive mixing via diffusion occurs across the interface of the two co-flowing streams. Once the transducer is actuated, micropost oscillations generate localized microvortices. Depending on the strength of these vortices relative to the external flow, the induced microstreaming flow can induce transverse advection and significantly enhance mixing performance.

To optimize mixing, we test devices with one, two, and three rows of microposts patterned across the channel width. Experiments using a single row of circular microposts along the centerline (results not shown) produce weak microvortices that are insufficient to achieve complete mixing within the desired flow rate range. Designs with two rows of microposts yield stronger mixing but fail to achieve a fully mixed regime. Here, the microvortices occur away from the interface of the two flows, essentially mixing fluids within the two flows separately with insufficient mixing occurring near the interface (see Video S4 and Fig. 3a, top).

Our finalized design features three rows of microposts patterned symmetrically across the width of the main channel. In this design, in addition to the two rows within each flow region, there is a third row positioned approximately along the centerline of the main channel, where the interface of the two flows aligns. The resultant microstreaming flow of this design disrupts the interface and induces mixing within both streams (see Video S5). When the microstreaming strength exceeds that of the external flow, the interface between the two fluids becomes highly disrupted at the exit of the main channel, resulting in a nearly uniform color distribution across the width of the channel (Fig. 3a, “PZT on”, bottom). To further characterize the fluid dynamics in our

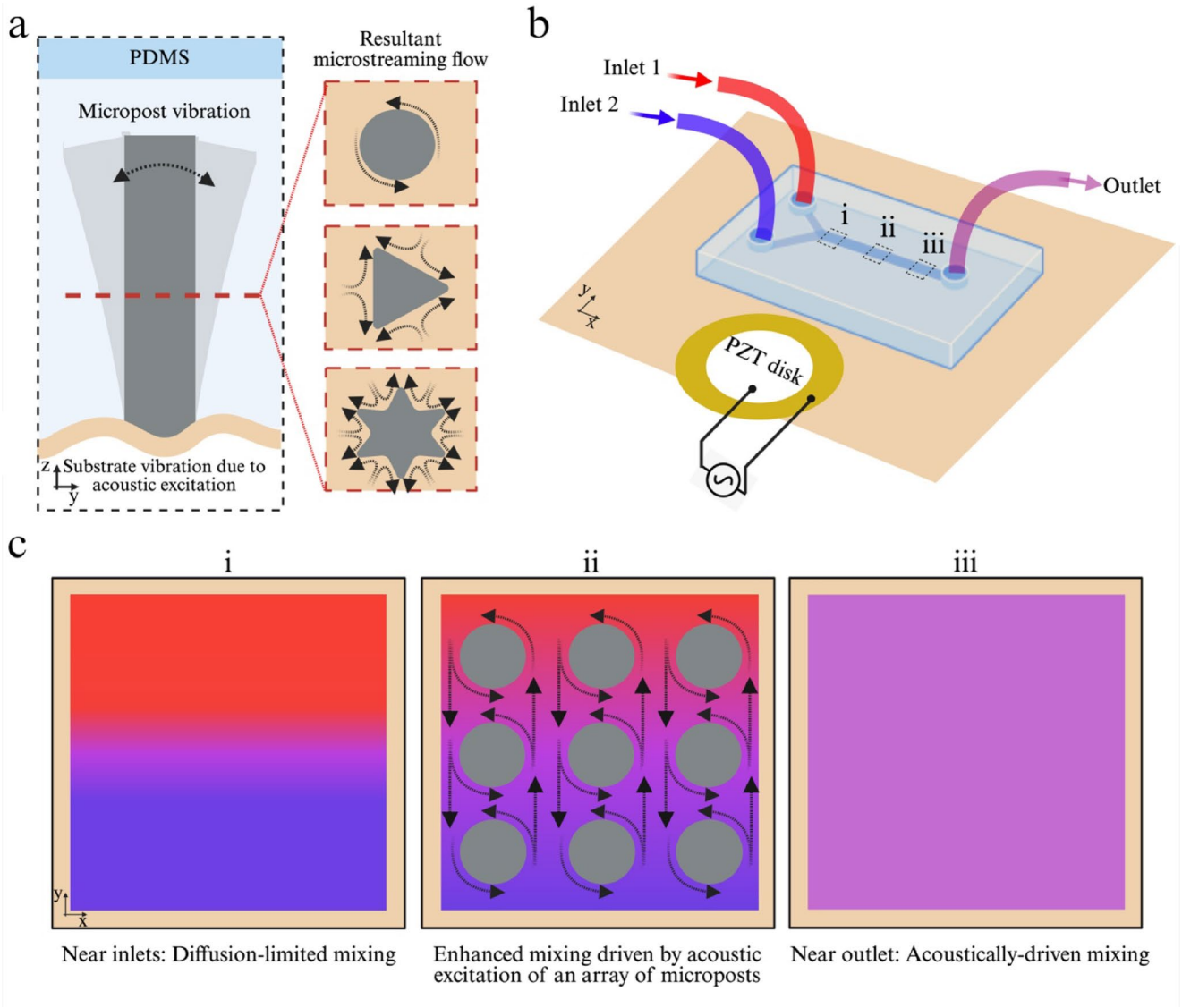

Fig. 2 Schematic diagrams illustrating the micropost geometry, device setup, and flow conditions. (**a**) Side-view of a single polymer micropost with a cylindrical shape (x–z plane), showing the small gap between the micropost's top and the channel ceiling that allows free vibration. The red dashed line indicates the cross-sectional shape of the micropost, exemplified here for three designs (circular, triangular, star). Arrows depict a micropost's deflection under acoustic excitation (left) and the expected microstreaming flow pattern (right). (**b**) Schematic of the acoustofluidic platform, featuring a Y-shaped PDMS microchannel (with two inlets merging into one outlet) bonded to a piezoelectric transducer. (**c**) Cross-sectional illustrations of the channel at three locations corresponding to panel (**b**): (i) near the channel inlets, showing two unmixed streams (red and blue) flowing in parallel; (ii) mid-channel (top view) with three rows of microposts, where acoustic microstreaming (curved arrows around each micropost) induces mixing between the streams; (iii) near the channel outlet, displaying a single fully mixed stream (purple) after effective microstreaming. All schematics are not to scale

device, we calculate the Reynolds and Peclet numbers under experimental flow conditions (see Supplementary Note 1). The Reynolds number, $Re \approx 1$, confirms laminar flow with comparable inertial and viscous forces. The Peclet number, $Pe \approx 10^4$, indicates a convection-dominated regime where diffusion alone is insufficient for efficient mixing. These values align with theoretical predictions for microfluidic systems and support the use of acoustically induced streaming flows to enhance transverse transport. Accordingly, the three-row configuration was selected for all subsequent mixing experiments.

We investigate the mixing result from various actuation conditions. We quantify the degree of mixing by calculating the mixing performance, φ, using the standard deviations of pixel intensities along a line across to the channel width (Figure S6). Initially, φ is assessed with the transducer off, allowing us to measure the baseline effect of passive diffusion on φ. In our three-row micropost configuration, the

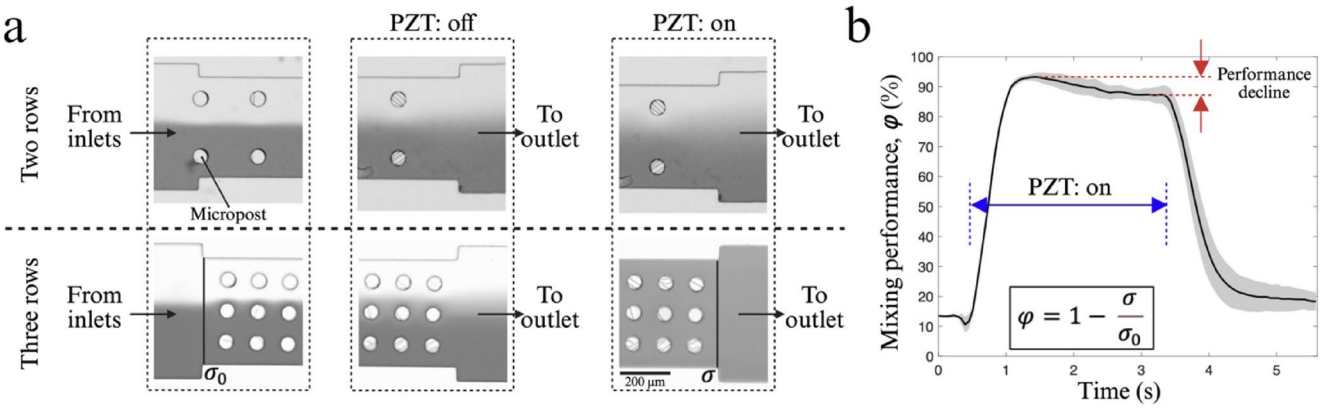

Fig. 3 Performance comparison between devices with two-row and three-row micropillars. (**a**) Microscopic images showing the entrance (left) and exit (middle and right) of the main channel for devices with two (top) and three (bottom) rows of micropillars. The flow direction is left to right, as indicated by black arrows. The irregular lines and curves on top of the microposts represent the surface roughness. As shown, only the three-row design produces a nearly homogeneous solution at the exit of the main channel. (**b**) Plot of mixing performance, φ, for the three-row design over one acoustic pulse. Solid lines in the bottom row of (**a**) indicate the locations where grayscale intensities are extracted for the calculation of φ using the equation overlaid onto (**b**). The data in (**b**) represent the average and standard deviation of two independent pulses on the same device. The duration of the transducer being on and the decline in mixing performance are indicted in (**b**) by blue and purple arrows, respectively. In both (**a**) and (**b**), a voltage of $118\ \mathrm{V_{pp}}$ and a flow rate of $10\ \mu\mathrm{L/min}$ are employed resulting in φ to increase from 9% and 11.6% (corresponding to "PZT: off") to 58% and 92.8% (corresponding to "PZT: on") for the two-row and three-row devices, respectively

interface of the flows is disrupted due to the presence of the microposts in the mid-section of the microchannel, where the interface would otherwise meet, resulting in slight mixing (Fig. 3a, "PZT off", bottom, middle).

We evaluate the impact of microstreaming on φ by comparing the results from transducer on vs. off. As shown in Fig. 3b and Video S5, the acoustic microstreaming flow generated by the transducer actuation causes a sharp rise in φ (within approximately 0.5 s). However, as the actuation continues and once φ reaches its maximum value, pressure builds up in the externally supplied flows, which leads to a slight increase in the flow rate. This pressure buildup temporarily disrupts the microstreaming flow, resulting in a slight reduction in mixing performance for the remainder of the time the transducer is on (see "performance decline" in Fig. 3b). Thermally induced degradation of the transducer's function may also contribute to this reduction in mixing performance. When the transducer is switched off, the mixing performance initially decreases sharply before gradually decaying to its basal value.

Even though the highest mixing performance exceeds $\varphi = 90\%$, it does not reach 100%. This may be due to the conservative method used to calculate φ, which uses the standard deviations σ and σ_o calculated when the transducer is on. Since the transducer's actuation can influence dye distribution at the entrance (see Figure S6.b) by reducing σ_o relative to the transducer-off case, calculating φ when the transducer is on could lead to an underestimation of φ when comparing it to the transducer-off condition.

C. Actuation voltage and flow rate: Investigating key factors affecting mixing performance

In our acoustofluidic device, a higher actuation voltage results in stronger substrate vibrations and, consequently, stronger vibrations of the microposts. By measuring the mixing performance at the midpoint of each pulse, we quantify φ for various conditions. As shown in Fig. 4a, a higher actuation voltage results in higher mixing performance, consistent with previous studies (Shah 2019; Zhao et al. 2021). This experimentally observed enhancement is further supported by theoretical considerations of acoustic microstreaming (see Supplementary Note 2). In our system, tracer particles are much smaller than the critical radius and therefore their motion is dominated by the Stokes drag force from acoustic streaming, which scales with the streaming velocity (Bruus 2012; Gor'Kov 1962). Since stronger micropost oscillations increase the streaming velocity in the surrounding fluid, the resulting drag on particles is enhanced, leading to more vigorous circulation and improved mixing performance. This trend is observed for microposts with different cross-sectional shapes, although circular microposts achieve the highest mixing performance, while the star-shaped ones result in the lowest, for all non-zero actuation voltages.

At zero voltage, the primary mechanism for mixing is diffusion. In the absence of microposts, the channel exhibits minimal mixing performance ($\approx 10\%$), as indicated by the green square markers in Fig. 4b. When microposts are introduced, the structures act as obstacles, causing the

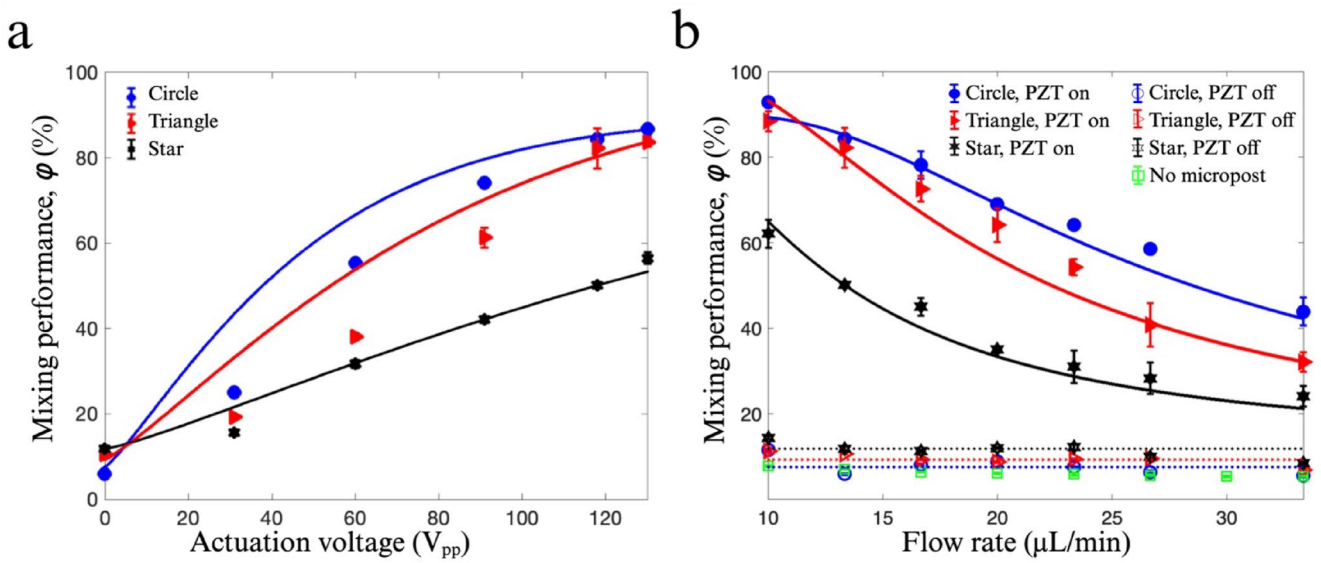

Fig. 4 Plots showing experimental measurements of mixing performance φ versus (**a**) actuation voltage and (**b**) flow rate. Experimental data (filled and unfilled markers) are overlaid with fitted curves (solid and dashed traces). The solid and dashed traces represent nonlinear least squares fits using an asymptotic exponential growth model, of the form: $? = a + b\left(1 - e^{\left[\frac{cV^d}{u_{ex}e}\right]}\right)$. (**a**) The effect of actuation voltage (peak-to-peak voltage) on mixing performance φ across microposts with different cross-sectional shapes (circle: blue circular markers, triangle: red triangular markers, star: black stars). In (**a**), the flow rate is fixed at 13.3 μL/min. When the transducer is off, the microposts act as obstacles. Upon activation of the transducer, microstreaming becomes the dominant mixing mechanism. Circular microposts show the highest mixing performance, while the star-shaped posts exhibit the lowest φ for non-zero actuation voltages. (**b**) The effect of flow rate on mixing performance across different shapes (circle: blue, triangle: red, star: black, no microposts: green squares) for two transducer conditions: "on", with V_{pp} = 118 V (filled markers, fit with solid traces), and "off" (unfilled markers, fit with dashed traces). When the transducer is off, microposts act as obstacles, leading to relatively low mixing. When the transducer is on, the primary mechanism is microstreaming flow, resulting in enhanced mixing. Error bars represent one standard deviation from three independent acoustic pulses; each performed on the same device under identical conditions with sufficient delay between pulses to avoid carryover effects.

fluid to bypass each micropost with varying levels of disruption. For example, circular microposts allow smooth bypass flow. In contrast, star-shaped microposts generate more flow resistance, potentially enhancing the likelihood of flow separation downstream as the flow bypasses each star-shaped micropost. Among the different shapes studied, the star-shaped microposts exhibit the highest passive mixing performance (11.8%), while the circular microposts show the lowest (5.9%). The smaller average edge-to-edge distance between two adjacent microposts for star-shaped microposts, measured at multiple points in the direction perpendicular to the channel, could increase the hydrodynamic resistance of the channel more than that of the circular microposts (see Figure S7 for average edge-to-edge distances for various shapes). This, in turn, may locally raise the velocities of the external flow, induce perturbations, and ultimately improve mixing.

When the transducer is turned on, the dominant mixing mechanism is the microstreaming flow. A smaller spacing between adjacent sharp edges along a channel wall can suppress the resultant acoustic streaming (Zhao et al. 2021). We observe a similar effect with star-shaped microposts, which perform poorly due to both their densely oriented sharp edges and the smaller average edge-to-edge distance between consecutive microposts. These factors lead to the lowest mixing performance φ among the three micropost shapes. Also, as discussed below, the directions of the microstreaming vortices vary for different shapes, which could also explain this discrepancy observed in the mixing performance.

Flow rate is another critical factor influencing mixing performance in microfluidic systems. According to the literature, higher flow rates in passive mixers lead to chaotic advection, disrupting the symmetry of Dean vortices and resulting in improved mixing performance in curved microchannels (Liao et al. 2021). However, lower flow rates in acoustic mixers lead to higher mixing performance by increasing the fluid residence time and reducing the suppression of microstreaming flow (Zhao et al. 2021). As shown in Fig.3b, reducing the flow rate increases the time fluid spends in the channel, leading to higher mixing performance for all different shapes. The circular microposts exhibit the highest mixing performance at each flow rate, while the star-shaped microposts demonstrate the lowest mixing performance. This difference is likely due to the average edge-to-edge distance necessary for creating effective microstreaming flow

between consecutive microposts. The triangular micropost is the most sensitive to flow rate changes, while the star-shaped microposts are the least sensitive.

Figure 4b compares the mixing performance φ with the transducer off (where diffusion is the primary mechanism) and with the transducer on (where both diffusion and microstreaming flow are at play). At lower flow rates, mixing performance φ deviates significantly from the transducer-off condition values across different shapes. This deviation may be due to the increased time the fluids are influenced by the microstreaming flows and the strong microstreaming relative to the external flow. At higher flow rates, however, the variations across different shapes are reduced, as the fluids are influenced by the microstreaming flows for a shorter time, and the microvortices are suppressed by the external flow. The observed difference between these two conditions underscores the significant impact of microstreaming flow on enhancing mixing performance.

In our acoustofluidic device, the mixing phenomenon between two fluids can be analyzed mathematically. When the transducer is on in our acoustofluidic device, two sources of fluid flow exist in the main channel that contribute simultaneously to the magnitude of the mixing performance, φ. One source is the externally supplied flow, and its resultant average velocity u_{ex}, which is controlled by the syringe pump. The other is the net acoustic microstreaming flow. Since in our system the transport of dye across the channel width influences φ, neglecting the diffusion effect, we can define two advection timescales to characterize this transport fully:

- $t_{ex} \propto \frac{1}{u_{ex}}$: This is the timescale of advection along the channel due to the externally supplied flow.
- $t_{ac} \propto \frac{1}{u_{ac}}$: This is the timescale of advection across the channel width due to the y-component (Fig. 2b–c) of the net acoustic microstreaming flow, u_{ac}, which correlates with the actuation voltage, V, as $u_{ac} \propto V^d$, where, under ideal conditions for bubble oscillations, the exponent $d = 2$ (Ahmed et al. 2016; Miller 1988).

In the absence of acoustic excitation, the transverse flow component u_{ac} is effectively zero due to the laminar and unidirectional nature of the flow. This absence prevents cross-stream transport. Acoustic microstreaming introduces a non-zero transverse velocity, enabling dye particles to move across streamlines and significantly enhance mixing efficiency. In our system, it is reasonable to assume that $? :\propto \frac{t_{ex}}{t_{ac}}$, which results in $? :\propto \frac{V^d}{u_{ex}}$. In addition, since φ can vary only between 0 and 100% and based on the observed behaviour of the experimental data, an asymptotic exponential growth model can be applied. Thus, we can write ? in the form of $? = a + b\left(1 - e^{\left[\frac{cV^d}{u_{ex}{}^e}\right]}\right)$, where a, b, c, d, and e are assumed to be constants for devices of each micropost shape and can be determined by fitting this equation to the experimental data. Using the MATLAB Curve Fitter tool, we combine all experimental data for mixing performance φ and conduct a "nonlinear least squares" fitting. As discussed above, from the physics of bubble-induced microstreaming flow and the laminar flow, we expect d and e to be close to 2 and 1, respectively. To impose this constraint, we set lower and upper limits for these two parameters in the Curve Fitter tool, with ranges of [1.8 2.2] and [0.8 1.2], respectively. This results in a fixed set of parameters (see Table S1) for each shape, which can roughly predict the behaviour of the devices with that particular shape under various conditions (i.e., constant flow rate, constant voltage, and PZT off; see Fig. 4).

D. Acoustic microstreaming flow pattern

To further understand the microstreaming flows generated by the microposts, we investigate the streaming patterns around different shapes of microposts in a quiescent liquid (i.e., when the external flow is stopped). In these experiments, we use 1 μm diameter polystyrene beads as tracer particles (Section II.C) to visualize the flow. At this small size, the acoustic radiation force on the beads is negligible, and thus the motion of beads is governed primarily by drag from the microstreaming flows (see Supplementary Note 2) (Barnkob et al. 2012; Carugo et al. 2014; Qiu et al. 2021; Salari et al. 2020; Tho et al. 2007). The microstreaming flow is recorded approximately at the mid-plane of the microposts, where the strongest microstreaming flow is observed (Fig. 5). All recordings are taken at the same imaging plane (mid-plane) set at a fixed height relative to the bottom substrate. Notably, the maximum microstreaming velocity occurs at this mid-plane (consistent with Salari et al. 2020). It is known that an acoustically driven bubble can exhibit various oscillation modes depending on its vibration pattern, resulting in four distinct microstreaming flow patterns: circular, elliptical, dipole, and quadrupole vortices (Tho et al. 2007). Similarly, in our experiments, we expect the emergence of various microstreaming patterns around the different shape microposts. Namely, we observe local pairs of microstreaming vortices near the vertices of triangular and star-shaped micropillars, and around the circular micropillars (Fig. 5a-c).

We note that there may be variations in the amplitude and direction of the vibration pattern in various regions inside the main channel. In addition, there may be fabrication defects in the microfluidic device and in the embedded microposts. Therefore, not all microposts in a single device are expected to generate the same microvortices. Under the applied acoustic excitation ($98\ \mathrm{kHz},\ 60\ \mathrm{V_{pp}}$), two predominant microstreaming patterns are observed around circular

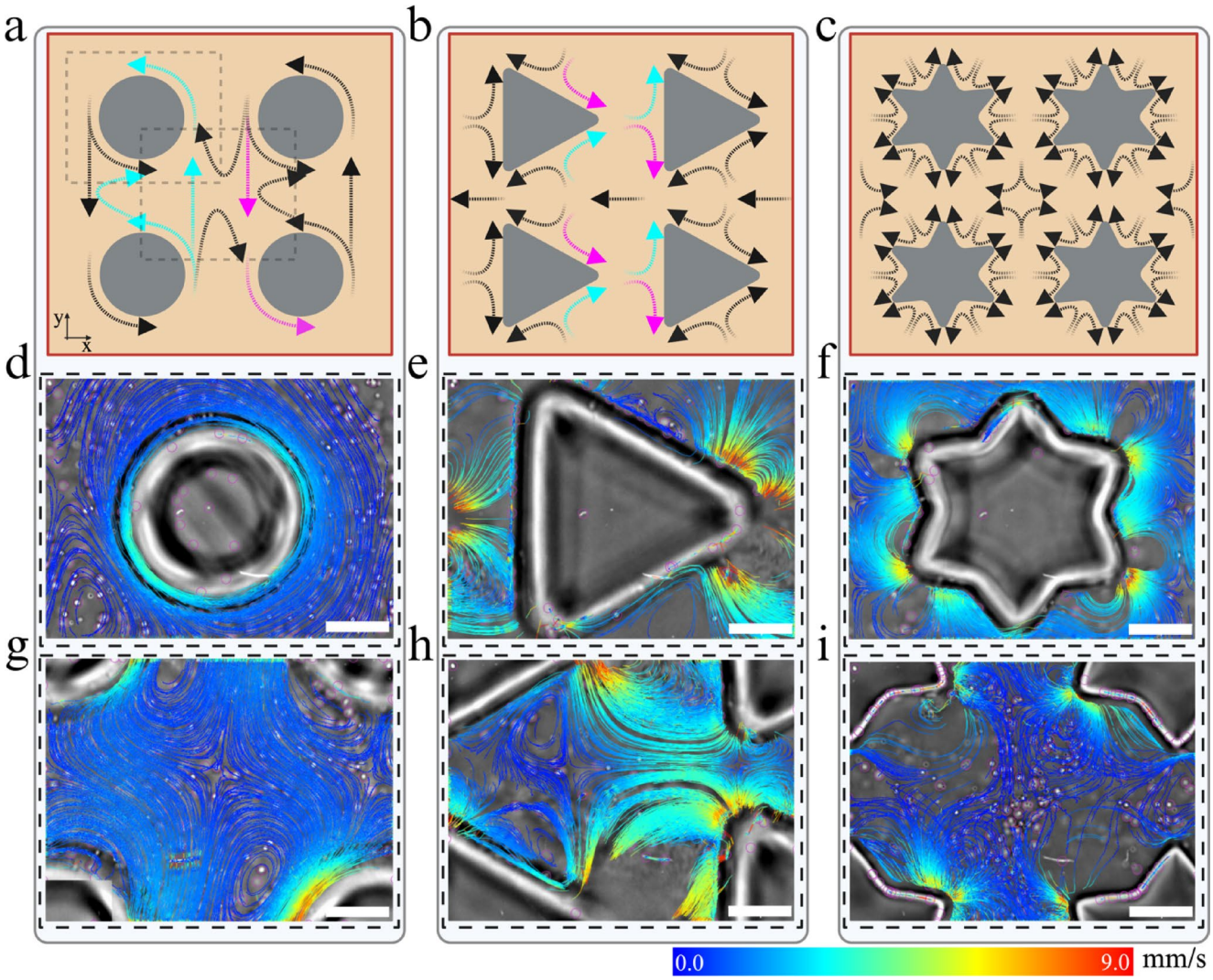

Fig. 5 Flow patterns of acoustic microstreaming generated by microposts with various cross-sectional shapes. (**a**–**c**) Schematic representations of the resultant microstreaming flow in a region of four (**a**) circular, (**b**) triangular, and (**c**) star-shaped microposts. For circular and triangular microposts, two sets of arrows representing net advections in y-direction are highlighted in cyan and magenta for +y and -y net flow directions, respectively. As shown, circular microposts exhibit dominant semi-symmetric circular vortices (black arrows circulating around each micropost), while triangular and star-shaped microposts display a semi-symmetrical vortex pair at each vertex of the pillars. (**d**–**i**) Microscopic images of microposts with the overlaid microstreaming flow estimates (colored lines) extracted from the bead tracking software for the regions outlined by two dashed square boxes in (**a**) surrounding a single micropost (**d**–**f**) and in the region between an array of four microposts (**g**–**i**). In (**d**–**i**), the scale bars are $20\ \mu m$, the color bar represents the velocity magnitude in mm/s, and an actuation voltage of 60 V_{pp} is used

microposts. The most common and reproducible pattern consists of a semi-symmetric circular vortex form centered around the micropost. In a smaller number of cases, a quadrupolar pattern—characterized by four distinct vortices—is observed (results not shown). Despite this variability, the semi-symmetric pattern remains dominant across devices and serves as the basis for all quantitative analyses in this study.

Figure 5d shows the microstreaming flow pattern and velocity magnitude around a circular micropost, demonstrating semi-symmetric circular vortices (see Video S6). In Fig. 5e, the microstreaming pattern around a triangular micropost reveals a pair of microvortices (one clockwise and one counterclockwise) around each triangle vertex (see Video S7). Similarly, Fig. 5f depicts the microstreaming pattern around a star-shaped micropost, demonstrating pairs of microvortices (two vortices countering each other) at four vertices on the right and left sides of the star-shaped micropost. However, the top and bottom vertices of the star do not generate noticeable microstreaming vortices, merely passing the fluid in a clockwise direction (see Video S8). This unexpected discrepancy may result from the microposts

being too close to the neighbouring pillars or the channel wall at the top and bottom, which may cause the suppression of the two pairs of microvortices.

To further investigate the effects of neighbouring microposts on the flow streamlines, we study the microstreaming in a square-shape region consisting of four microposts at its corners, arranged in two consecutive rows and columns. For circular microposts, the vortices of each micropost appear to influence the neighbouring ones resulting in the microstreaming around the microposts to become less symmetric (Fig. 5g), while still roughly resembling the expected flow directions. Furthermore, due to the varying edge-to-edge spacing between adjacent microposts (Figure S7), additional clockwise vortices form in the region between the circular microposts (see Video S9). Each of the four triangular microposts creates a pair of opposing vortices around each vertex (Fig. 5h). The proximity of adjacent microposts leads to the formation of new vortices along the slant edge of the micropost (see Video S10). Figure 5i displays the microstreaming pattern between four star-shaped microposts, indicating pairs of microvortices around four vertices on the right and left sides of the star-shaped micropost (see Video S11).

Interestingly, the average of the maximum tracer velocities around the microposts was measured to be $8.88 \pm 1.29 \, {}^{\mathrm{mm}}/_{\mathrm{s}}$ under identical acoustic excitation conditions ($98\, kHz,\ 60\, V_{pp}$). This average value was consistent across different micropost geometries and across multiple devices. The streaming velocity was determined from tracer motion using the same measurement protocol described in our previous work (Salari et al. 2020), which is also cited here. The R script for this analysis is provided in Supplementary File 2. However, as discussed above, the mixing performance is highest for circular microposts and lowest for star-shaped microposts (Fig. 4). This can be partially attributed to the larger void spaces between circular microposts compared to those for triangular and star-shaped ones (Fig. 5a-c) resulting in the inhibition of the formation of constructive microvortices for the star-shaped microposts. In addition, for the circular and the triangular microposts, the superposition of microvortices generated by individual posts can result in a net advection across the width of the channel. This is illustrated schematically in Fig. 5a-b, where the curved arrows, highlighted in cyan and magenta, represent the net advection in the +y and -y directions, respectively. For the star-shaped microposts, however, the formation of such net advection is largely suppressed. This lateral advection facilitates the flow from one circular or triangular micropost to the next adjacent one in the y direction, enhancing the transport of dye across the width of the main channel and ultimately improving mixing performance. Although star-shaped microposts generate a larger number of local microvortices per pillar—which may promote local mixing—these vortices primarily interfere, limiting effective transport across the channel width.

These observed differences in mixing performance may be further explained by considering the resistance to bending of each micropost shape, quantified by the second moment of inertia (MOI). The MOI reflects a structure's resistance to bending under acoustic excitation. Among the three shapes, circular microposts have the lowest MOI, which may contribute to greater oscillation amplitude and thus stronger microstreaming. Triangular microposts, with their rigid angular geometry, exhibit a moderately higher MOI and may lead to correspondingly weaker streaming. Star-shaped microposts have the highest MOI due to their extended, vertex-rich structure, making them the most resistant to vibration. This resistance to bending limits the microposts' deflection, which may result in weaker and less effective microstreaming. Indeed, the trend in mixing performance—highest for circular, moderate for triangular, and lowest for star-shaped microposts—appears to scale inversely with the microposts' MOI (see Supplementary Note 3).

4 Conclusion

This study investigates the mixing performance of microfluidic micropost-driven acoustic mixers by examining the influence of micropost shape, actuation voltage, and flow rate. Photocrosslinkable polymers are used to fabricate the microposts with high geometric precision. The primary novelty of this work lies in the systematic evaluation of how micropost cross-sectional shape affects acoustic microstreaming and mixing performance. Among the shapes studied, we find that circular microposts achieve the highest mixing efficiency, with a mixing performance $\varphi = 86.7\%$. We attribute this performance to its ability to produce stronger advection across the width of the channel and its optimal spacing between adjacent edges, forming more constructive microvortices. In contrast, star-shaped microposts exhibit the lowest mixing performance ($\varphi = 56.5\%$). Although the sharp edges of star-shaped microposts enhances microstreaming locally, the smaller void volume between neighbouring microposts likely suppresses the formation of constructive acoustic streaming. Triangular microposts produce moderate mixing performance.

The results of this study reinforce those of previous studies, demonstrating that higher actuation voltages increase substrate vibrations, leading to stronger microstreaming flows and enhanced mixing performance across all micropost shapes. Lower flow rates also improve mixing by allowing more time for diffusion and enhancing microstreaming effects. Additionally, circular microposts

consistently outperform other shapes, while star-shaped microposts are the least effective. Detailed microstreaming analysis shows that circular microposts create semi-symmetrical circular vortices, triangular microposts generate two opposing vortices at each vertex, and star-shaped microposts form opposing vortices at four points with minimal microstreaming flow at the top and bottom. Although the magnitude of the microstreaming flow velocity is approximately the same across different shapes and devices ($8.88 \pm 1.29\,{}^{\mathrm{mm}}/_{\mathrm{s}}$), the other differences between the different shapes result in different overall mixing performances. Our analysis of micropost geometry suggests that circular posts, which have the lowest MOI, may allow greater deflection and oscillation amplitude under acoustic excitation. In contrast, star-shaped microposts have the highest MOI, which may contribute to reduced micropost oscillation. The microposts' geometric resistance to bending appears to be consistent with our observed trends in mixing performance, whereby circular posts outperform triangular and star-shaped posts due to stronger microstreaming.

In summary, we find the design and arrangement of the microposts in such microfluidic mixers to be crucial factors in enhancing the performance of the mixers. These insights provide valuable guidance for designing more efficient microfluidic mixing devices for applications requiring precise and rapid mixing. Future work may explore additional micropost geometries and configurations and integrate these findings into biomedical applications such as nanoparticle synthesis, cargo delivery to cells, and biosensing.

Supplementary Information The online version contains supplementary material available at https://doi.org/10.1007/s10404-025-02845-0.

Acknowledgements This research was partially supported by the Natural Sciences and Engineering Research Council of Canada (NSERC) Discovery Grants program (RGPIN-2019-04618), the Canadian Institutes of Health Research (CIHR) Project Grants program (202303PJT-496149-BE2ABAF-244211), and equipment funding from the Canada Foundation for Innovation (CFI, projects 36687 and 36442), the Ontario Research Fund (ORF), and Toronto Metropolitan University, awarded to S.S.H.T. Additional funding was provided by the NSERC Discovery Grants program (RGPIN-2022-04143), equipment funding from CFI (project 30994), and the Ontario Research Fund—Research Excellence (ORF-RE #RE02-032), all awarded to M.C.K. Figures were created in Biorender.com. The authors would like to acknowledge the Keenan Research Centre for Biomedical Science Core Facilities at St. Michael's Hospital. Special thanks to Dr. Muhammad Saad Khan, Niloofar Ghasemzaie, and Steven Tran for their technical assistance on the project.

Author contributions B.C. fabricated the microfluidic devices, conducted all acoustofluidic experiments, and ran the data analysis. S.J. fabricated the micropillar arrays. B.C., A.S., M.C.K., and S.S.H.T. conceptualized the idea. B.C. and A.S. designed the experiments, generated figures, and wrote the manuscript draft. Z.L.H wrote the R scripts for automated analysis. A.R.W., D.K.H., M.C.K., and S.S.H.T. secured funding for the study and provided supervision. All authors contributed to the discussion of the results.

Data availability The data used in this study can be obtained from the corresponding author upon reasonable request.

Declarations

Competing interests The authors declare no competing interests.

References

Ahmed H, Rezk AR, Richardson JJ, Macreadie LK, Babarao R, Mayes ELH, Lee L, Yeo LY (2019) Acoustomicrofluidic assembly of oriented and simultaneously activated metal–organic frameworks. Nat Commun 10(1):2282. https://doi.org/10.1038/s41467-019-10173-5

Ahmed D, Mao X, Juluri BK, Huang TJ (2009) A fast microfluidic mixer based on acoustically driven sidewall-trapped microbubbles. Microfluid Nanofluidics 7(5):727–731. https://doi.org/10.1007/s10404-009-0444-3

Ahmed D, Ozcelik A, Bojanala N, Nama N, Upadhyay A, Chen Y, Hanna-Rose W, Huang TJ (2016) Rotational manipulation of single cells and organisms using acoustic waves. Nat Commun 7(1):11085. https://doi.org/10.1038/ncomms11085

Barnkob R, Augustsson P, Laurell T, Bruus H (2012) Acoustic radiation- and streaming-induced microparticle velocities determined by microparticle image velocimetry in an ultrasound symmetry plane. Phys Rev E 86(5):056307. https://doi.org/10.1103/PhysRevE.86.056307

Beebe DJ, Mensing GA, Walker GM (2002) Physics and applications of microfluidics in biology. Annu Rev Biomed Eng 4:261–286. https://doi.org/10.1146/annurev.bioeng.4.112601.125916

Bruus H (2012) Acoustofluidics 7: the acoustic radiation force on small particles. Lab Chip 12(6):1014–1021. https://doi.org/10.1039/C2LC21068A

Cai G, Xue L, Zhang H, Lin JA, Review on (2017) Micromixers Micromachines 8(9):274. https://doi.org/10.3390/mi8090274

Carugo D, Octon T, Messaoudi W, Fisher AL, Carboni M, Harris NR, Hill M, Glynne-Jones PA (2014) Thin-reflector microfluidic resonator for continuous-flow concentration of microorganisms: a new approach to water quality analysis using acoustofluidics. Lab Chip 14(19):3830–3842. https://doi.org/10.1039/C4LC00577E

Cha B, Lee SH, Iqrar SA, Yi H-G, Kim J, Park J (2023) Rapid acoustofluidic mixing by ultrasonic surface acoustic wave-induced acoustic streaming flow. Ultrason Sonochem 99:106575. https://doi.org/10.1016/j.ultsonch.2023.106575

Chen Z, Shen L, Zhao X, Chen H, Xiao Y, Zhang Y, Yang X, Zhang J, Wei J, Hao N (2022) Acoustofluidic micromixers: from rational design to lab-on-a-chip applications. Appl Mater Today 26:101356. https://doi.org/10.1016/j.apmt.2021.101356

Debroy D, Oakey J, Li D (2018) Interfacially-mediated oxygen inhibition for precise and continuous poly(ethylene glycol) diacrylate (PEGDA) particle fabrication. J Colloid Interface Sci 510:334–344. https://doi.org/10.1016/j.jcis.2017.09.081

Ebadi A, Farshchi Heydari MJ, Toutouni R, Chaichypour B, Fathipour M, Jafari K (2019) Efficient paradigm to enhance particle separation in deterministic lateral displacement arrays. SN Appl Sci 1(10):1184. https://doi.org/10.1007/s42452-019-1064-5

Ershov D, Phan M-S, Pylvänäinen JW, Rigaud SU, Le Blanc L, Charles-Orszag A, Conway JRW, Laine RF, Roy NH, Bonazzi D, Duménil G, Jacquemet G, Tinevez J-Y (2022) Trackmate 7:

integrating state-of-the-art segmentation algorithms into tracking pipelines. Nat Methods 19(7):829–832. https://doi.org/10.1038/s41592-022-01507-1

Hakimi N, Tsai SSH, Cheng C-H, Hwang DK (2014) One-step two-dimensional microfluidics-based synthesis of three-dimensional particles. Adv Mater 26(9):1393–1398. https://doi.org/10.1002/adma.201304378

Harley WS, Kolesnik K, Heath DE, Collins DJ (2024) Enhanced acoustic streaming effects via sharp-edged 3D microstructures. Lab Chip 24(6):1626–1635. https://doi.org/10.1039/D3LC00742A

Hejazian M, Nguyen N-TA, Rapid Magnetofluidic (2017) Micromixer Using Diluted Ferrofluid Micromachines 8(2):37. https://doi.org/10.3390/mi8020037

Huang P-H, Xie Y, Ahmed D, Rufo J, Nama N, Chen Y, Chan CY, Huang TJ (2013) An acoustofluidic micromixer based on oscillating sidewall sharp-edges. Lab Chip 13(19):3847–3852. https://doi.org/10.1039/C3LC50568E

Juraeva M, Kang D-J (2023) Mixing performance of a passive micromixer based on multiple baffles and submergence scheme. Micromachines 14(5):1078. https://doi.org/10.3390/mi14051078

Kim TH, Lee JM, Ahrberg CD, Chung BG (2018) Development of the microfluidic device to regulate shear stress gradients. Biochip J 12(4):294–303. https://doi.org/10.1007/s13206-018-2407-9

Lee C-Y, Chang C-L, Wang Y-N, Fu L-M (2011) Microfluidic mixing: a review. Int J Mol Sci 12(5):3263–3287. https://doi.org/10.3390/ijms12053263

Li Z, Zhang B, Dang D, Yang X, Yang W, Liang W (2022) A review of microfluidic-based mixing methods. Sensors and Actuators A: Physical 344:113757. https://doi.org/10.1016/j.sna.2022.113757

Li M, Joung D, Kozinski JA, Hwang DK (2017) Fabrication of highly porous nonspherical particles using stop-flow lithography and the study of their optical properties. Langmuir 33(1):184–190. https://doi.org/10.1021/acs.langmuir.6b03358

Liao Y, Mechulam Y, Lassalle-Kaiser BA (2021) A millisecond passive micromixer with low flow rate, low sample consumption and easy fabrication. Sci Rep 11(1):20119. https://doi.org/10.1038/s41598-021-99471-x

Lim H, Back SM, Choi H, Nam J (2019) Acoustic mixing in a dome-shaped chamber-based SAW (DC-SAW) device. Lab Chip 20(1):120–125. https://doi.org/10.1039/C9LC00820A

Lu Y, Zhang M, Zhang H, Huang J, Wang Z, Yun Z, Wang Y, Pang W, Duan X, Zhang H (2018) On-chip acoustic mixer integration of electro-microfluidics towards in-situ and efficient mixing in droplets. Microfluid Nanofluid 22(12):146. https://doi.org/10.1007/s10404-018-2169-7

Lu Y, Tan W, Mu S, Zhu G (2024) Vortex-enhanced microfluidic chip for efficient mixing and particle capturing combining acoustics with inertia. Anal Chem 96(9):3859–3869. https://doi.org/10.1021/acs.analchem.3c05291

Lu Y, Tan W, Mu S, Zhu GA, Multi-Vortex (2023) Micromixer based on the synergy of acoustics and inertia for nanoparticle synthesis. Anal Chim Acta 1239:340742. https://doi.org/10.1016/j.aca.2022.340742

Luong T-D, Phan V-N, Nguyen N-T (2010) High-Throughput micromixers based on acoustic streaming induced by surface acoustic wave. https://doi.org/10.1007/s10404-010-0694-0

Ma Z, Teo AJT, Tan SH, Ai Y, Nguyen N-T (2016) Self-aligned interdigitated transducers for acoustofluidics. Micromachines 7(12):216. https://doi.org/10.3390/mi7120216

Miller DL (1988) Particle gathering and microstreaming near ultrasonically activated gas-filled micropores. J Acoust Soc Am 84(4):1378–1387. https://doi.org/10.1121/1.396636

Moon B-U, Tsai SSH, Hwang DK (2015) Rotary polymer micromachines: in situ fabrication of microgear components in microchannels. Microfluid Nanofluidics 19(1):67–74. https://doi.org/10.1007/s10404-015-1548-6

Nair MP, Teo AJT, Li KHH (2022) Acoustic biosensors and microfluidic devices in the decennium: principles and applications. Micromachines 13(1):24. https://doi.org/10.3390/mi13010024

Nama N, Huang P-H, Huang TJ, Costanzo F (2016) Investigation of micromixing by acoustically oscillated sharp-edges. Biomicrofluidics 10(2):024124. https://doi.org/10.1063/1.4946875

Orbay S, Ozcelik A, Lata J, Kaynak M, Wu M, Huang TJ (2017) Mixing high-viscosity fluids via acoustically driven bubbles. J Micromech Microeng 27(1):015008

Orbay S, Ozcelik A, Bachman H, Huang TJ (2018) Acoustic actuation of in situ fabricated artificial cilia. J Micromech Microeng 28(2):025012. https://doi.org/10.1088/1361-6439/aaa0ae

Park KJ, Lee KG, Seok S, Choi BG, Lee M-K, Park TJ, Park JY, Kim DH, Lee SJ (2014) Micropillar arrays enabling single microbial cell encapsulation in hydrogels. Lab Chip 14(11):1873–1879. https://doi.org/10.1039/C4LC00070F

Pawinanto RE, Yunas J, Hashim AM (2020) Micropillar based active microfluidic mixer for the detection of glucose concentration. Microelectron Eng 234:111452. https://doi.org/10.1016/j.mee.2020.111452

Pothuri C, Azharudeen M, Subramani K (2019) Rapid mixing in microchannel using standing bulk acoustic waves. Phys Fluids 31(12):122001. https://doi.org/10.1063/1.5126259

Qiu W, Joergensen JH, Corato E, Bruus H, Augustsson P (2021) Fast microscale acoustic streaming driven by a temperature-gradient-induced nondissipative acoustic body force. Phys Rev Lett 127(6):064501. https://doi.org/10.1103/PhysRevLett.127.064501

Rasouli MR, Tabrizian M (2019) An ultra-rapid acoustic micromixer for synthesis of organic nanoparticles. Lab Chip 19(19):3316–3325. https://doi.org/10.1039/C9LC00637K

Raza W, Hossain S, Kim K-Y (2020) A review of passive micromixers with a comparative analysis. Micromachines 11(5):455. https://doi.org/10.3390/mi11050455

Salari A, Dalton C (2019) Simultaneous pumping and mixing of biological fluids in a double-array electrothermal microfluidic device. Micromachines 10(2):92. https://doi.org/10.3390/mi10020092

Salari A, Appak-Baskoy S, Coe IR, Tsai SSH, Kolios MC (2021) An ultrafast enzyme-free acoustic technique for detaching adhered cells in microchannels. RSC Adv 11(52):32824–32829. https://doi.org/10.1039/D1RA04875A

Salari A, Appak-Baskoy S, Ezzo M, Hinz B, Kolios MC, Tsai SS (2020) H. Dancing with the cells: acoustic microflows generated by oscillating cells. Small Weinh Bergstr Ger 16(9):e1903788. https://doi.org/10.1002/smll.201903788

Salari A, Appak-Baskoy S, Coe IR, Abousawan J, Antonescu CN, Tsai SSH, Kolios MC (2021) Dosage-controlled intracellular delivery mediated by acoustofluidics for lab on a chip applications. Lab Chip 21(9):1788–1797. https://doi.org/10.1039/D0LC01303J

Shah I, Su Jeon H, Ali M, Yang DH, Choi K-H (2019) Optimal Parametric Mixing Analysis of Active and Passive Micromixers Using Taguchi Method. *Proc. Inst. Mech. Eng. Part E 233* (6), 1292–1303. https://doi.org/10.1177/0954408919862997

Stroock AD, Dertinger SKW, Ajdari A, Mezic I (2002) al, et. Chaotic mixer for microchannels. Science 295(5555):647–651

Tho P, Manasseh R, Ooi A (2007) Cavitation microstreaming patterns in single and multiple bubble systems. J Fluid Mech 576:191–233. https://doi.org/10.1017/S0022112006004393

Tian C, Liu W, Zhao R, Li T, Xu J, Chen S-W, Wang J (2018) Acoustofluidics-based enzymatic constant determination by rapid and stable in situ mixing. Sens Actuators B Chem 272:494–501. https://doi.org/10.1016/j.snb.2018.05.149

Tsai R-T, Wu C-Y (2011) An efficient micromixer based on multidirectional vortices due to baffles and channel curvature. Biomicrofluidics 5(1):014103. https://doi.org/10.1063/1.3552992

Wang X, Liu Z, Cai Y, Wang B, Luo XA (2021) Cost-Effective serpentine micromixer utilizing ellipse curve. Anal Chim Acta 1155:338355. https://doi.org/10.1016/j.aca.2021.338355

Wu M, Gao Y, Ghaznavi A, Zhao W, Xu J (2022) AC electroosmosis micromixing on a lab-on-a-foil electric microfluidic device. Sens Actuators B Chem 359:131611. https://doi.org/10.1016/j.snb.2022.131611

Xia Y, Whitesides GM, Soft Lithography (1998) Angew Chem Int Ed 37(5):550–575. https://doi.org/10.1002/(SICI)1521-3773(19980316)37:5%3C550::AID-ANIE550%3E3.0.CO;2-G

Xia Y, Whitesides GM (1998) SOFT LITHOGRAPHY. Annu Rev Mater Res 28(28, 1998):153–184. https://doi.org/10.1146/annurev.matsci.28.1.153

Xie Y, Nama N, Li P, Mao Z, Huang P-H, Zhao C, Costanzo F, Huang TJ (2016) Probing cell deformability via acoustically actuated bubbles. Small Weinh Bergstr Ger 12(7):902–910. https://doi.org/10.1002/smll.201502220

Yang F, Zhao W, Kuang C, Wang G (2021) Rapid AC electrokinetic micromixer with electrically conductive sidewalls. Micromachines 13(1):34. https://doi.org/10.3390/mi13010034

Yuk H, Zhang T, Lin S, Parada GA, Zhao X (2016) Tough bonding of hydrogels to diverse non-porous surfaces. Nat Mater 15(2):190–196. https://doi.org/10.1038/nmat4463

Zaheri-Ghannad S, Kordzadeh-Kermani V, Madadelahi M (2024) Cell/particle manipulation using bulk acoustic waves (BAWs) on centrifugal microfluidic platforms: a mathematical study. Chem Eng Process - Process Intensif 205:110024. https://doi.org/10.1016/j.cep.2024.110024

Zhang Y, Devendran C, Lupton C, Marco A (2019) Versatile platform for performing protocols on a chip utilizing surface acoustic wave (SAW) driven mixing. Lab Chip 19(2):262–271. https://doi.org/10.1039/C8LC01117F. NeildA.

Zhao S, Huang P-H, Zhang H, Rich J, Bachman H, Ye J, Zhang W, Chen C, Xie Z, Tian Z, Kang P, Fu H, Huang TJ (2021) Fabrication of tunable, high-molecular-weight polymeric nanoparticles via ultrafast acoustofluidic micromixing. Lab Chip 21(12):2453–2463. https://doi.org/10.1039/D1LC00265A

Zhou W, Niu L, Cai F, Li F, Wang C, Huang X, Wang J, Wu J, Meng L, Zheng H (2016) Spatial selective manipulation of microbubbles by tunable surface acoustic waves. Biomicrofluidics 10(3):034121. https://doi.org/10.1063/1.4954934

Munaz, A., Kamble, H., Shiddiky, M. J., & Nguyen, N. T. (2017).Magnetofluidic micromixer based on a complex rotating magnetic field - RSC Advances,7(83), 52465-52474. https://pubs.rsc.org/en/content/articlelanding/2017/ra/c7ra08073e

Li M, Hwang DK, Kozinski J (2015) Polymer Sheet Patterning and Its Assembly Using Slit Channel Lithography. US20150079523A1, March 19, https://patents.google.com/patent/US20150079523A1/en (accessed 2025-03-19).

Gor'Kov LP ((1962) *) On the Forces Acting on a Small Particle in an Acoustical Field in an Ideal Fluid. Soviet Physics Doklady, 6, 773. - References - Scientific Research Publishing*. https://www.scirp.org/reference/referencespapers?referenceid=2380435 (accessed 2025-09-03)